Energy & Environmental Science

ROYAL SOCIETY OF CHEMISTRY

PAPER

View Article Online
View Journal | View Issue

Cite this: *Energy Environ. Sci.*, 2024, **17**, 7372

Identifying iodide-ion regulation of early-stage zinc nucleation and growth for high-rate anode-free zinc metal batteries†

Wenchao Shi,‡[a] Zhenjun Song,‡[b] Wenwei Zhang,[a] Sitian Lian,[a] Fuzhi Huang,[a] Qinyou An *[a] and Qi Li *[c]

Anode-free aqueous zinc (Zn) metal batteries (AZMBs) have the advantage of providing higher energy density. However, without excess Zn metal, their cycling life is highly dependent on the reversibility of Zn deposition/dissolution, which is influenced by interfacial issues such as Zn dendrite formation and parasitic side reactions. A simple approach is developed to tackle this challenge by introducing lithium iodide as an additive to the electrolyte, where iodide ions (I^-) play a crucial role in regulating the early-stage Zn nucleation and growth. Initially, the formation of an I^--rich electrochemical double layer reduces the Marcus charge transfer energy barrier of Zn ions (Zn^{2+}), hence significantly lowering the heterogeneous nucleation overpotential of Zn. Subsequently, I^- ions are preferentially adsorbed onto the Zn (100) and Zn (101) crystal planes compared to the Zn (002) plane, thereby promoting the Zn growth onto these two planes and leading to Zn plating with the dominating Zn (002) orientation. As a result, highly reversible Zn deposition/dissolution is achieved in the Zn‖copper battery, with a superior initial and average coulombic efficiency of 99.9%. Moreover, the anode-free Zn‖iodine battery demonstrates excellent cycling stability and ultra-high-rate performance (0.99 mA h cm^{-2} capacity retained corresponding to an 88.2% retention after 10 000 cycles at 50 mA cm^{-2}). The I^- regulation strategy for early-stage Zn nucleation and growth behavior provides a simple and innovative approach to improving the Zn deposition/dissolution interfacial stability and hence the cycling stability and rate capability of anode-free AZMBs and can also be extended to other anode-free metal batteries.

Received 25th June 2024,
Accepted 21st August 2024

DOI: 10.1039/d4ee02784a

rsc.li/ees

Broader context

Aqueous zinc (Zn) metal batteries (AZMBs) are considered as one of the most promising energy storage technologies for stationary storage and micropower systems, owing to their advantages of low cost, high safety, and large theoretical capacity. However, conventional AZMBs suffer from low energy density due to the use of an unlimited Zn reservoir as the anode. Designing AZMBs with an anode-free structure can potentially achieve higher energy density. However, the cycling life of such batteries heavily depends on the reversibility of Zn deposition/dissolution, which is influenced by interfacial issues such as Zn dendrite formation and the hydrogen evolution reaction. Herein, we demonstrate that the interfacial specific adsorption behavior of iodide ions effectively regulates the early nucleation and growth of Zn, through enhancing the nucleation rate of Zn and initiating a predominant Zn (002) orientation during electrodeposition. This significantly improved the charge-transfer kinetics of Zn deposition and the interfacial stability of Zn deposition/dissolution, thereby leading to the anode-free Zn‖iodine battery with long-term cycling stability and high-rate performance. This work provides valuable insights into the design of other anode-free metal batteries.

Introduction

The progress of aqueous zinc (Zn) metal batteries (AZMBs) has been extraordinary, drawing a tremendous amount of interest.[1–3] The key reasons include the inherent safety and ecological attributes of aqueous electrolytes, low cost of Zn metal, and a high theoretical capacity (5855 mA h cm^{-3} or 820 mA h g^{-1}), along with a fairly suitable electrode potential (−0.76 V *vs.* standard hydrogen electrode).[4,5] However, the Zn metal anode still faces a series of

[a] *State Key Laboratory of Advanced Technology for Materials Synthesis and Processing, Wuhan University of Technology, Wuhan, 430070, P. R. China. E-mail: anqinyou86@whut.edu.cn*
[b] *School of Pharmaceutical and Materials Engineering, Taizhou University, Taizhou, 318000, P. R. China*
[c] *National Energy Key Laboratory for New Hydrogen-Ammonia Energy Technologies, Foshan Xianhu Laboratory, Foshan 528200, P. R. China. E-mail: liqi1@xhlab.cn*

† Electronic supplementary information (ESI) available. See DOI: https://doi.org/10.1039/d4ee02784a

‡ Equal contribution.

issues, such as the parasitic side reactions and dendritic formation at the Zn anode/electrolyte interface, leading to unsatisfied Zn deposition/dissolution reversibility.[6] To compensate for the insufficient reversibility, Zn metal is commonly used as the anode in laboratories, which provides a nearly limitless Zn reservoir to enhance the cycling stability of AZMBs.[7] However, this approach does not accurately reflect the batteries' performance in practical applications and significantly limits the real energy density. Anode-free AZMBs with no excess Zn metal have thus emerged and are more advantageous for practical applications due to their ability to provide a higher energy density. However, the cycling life of anode-free AZMBs is heavily dependent on the reversibility of Zn deposition/dissolution.[8]

Recent studies widely report the strategies for enhancing the deposition/dissolution reversibility of the Zn anode by manipulating electrolytes, including salt-in-water electrolytes, eutectic electrolytes, additives, *etc.*[9–11] Among these advances, additive engineering stands out and has attracted significant attention due to its simplicity, scalability, and remarkable effectiveness.[12–15] It is worth noting that most of these modifications have yet to be evaluated in anode-free AZMBs. Zn anode, like all other metal anodes, exhibits a dynamically renewed electrochemical deposition/dissolution interface during charge–discharge. Previous reports on lithium deposition/dissolution have demonstrated that early-stage metal nucleation and growth plays a crucial role in regulating the frontier morphology of the plated metal and suppressing the metal dendrite formation, although the underlying early-stage lithium nucleation and growth theory/model varies.[16–18] Whereas Zn metal has a hexagonal close-packed structure with three atomic packing crystal planes of Zn (002), Zn (100) and Zn (101) (Fig. S1, ESI†). The regulation of the early-stage Zn nucleation and growth towards one specific crystal plane orientation is favorable for realizing the ordered Zn growth in the following deposition process, maintaining the stability of dynamically renewed interfacial structure and hence the Zn deposition/dissolution reversibility. The early-stage Zn nucleation and growth regulation is particularly important for anode-free AZMBs, as the initial heterogeneous Zn nucleation and growth occurs on the surface of the current collector which has a significantly different nature from Zn. Additive engineering provides a facile way to regulate the early-stage Zn deposition process *via* electrode/electrolyte interfacial modification.[19–21] The currently proposed mechanisms for additive modification mainly involve two key aspects: the regulation of the electric double layer (EDL) and the solvated sheath structure. However, it remains elusive regarding how these two aspects influence the charge transfer process of Zn ions (Zn^{2+}) and subsequently the Zn deposition behavior. According to the Marcus theory, most investigations about the charge transfer mechanism have an underlying assumption that each electron must transfer separately.[22] This implies that the charge transfer process of Zn^{2+} involves two steps: the initial generation of a monovalent Zn^{+} intermediate, followed by its conversion to a Zn atom.[23,24] The first step is commonly considered the rate-determining step for the Zn deposition process.[23] Therefore, seeking high-efficiency additives and identifying the mechanism for regulating the Zn^{2+} charge transfer process and early-stage Zn deposition behavior are crucial for developing anode-free AZMBs.

Herein, a simple approach to achieve high-performance AZMBs by iodide ion (I^-) interfacial regulation was demonstrated. Lithium iodide (LiI) was selected as the source of I^-. The experimental results of attenuated total reflection Fourier transform infrared (ATR-FTIR), Raman, and nuclear magnetic resonance (NMR) spectroscopy together with molecular dynamics (MD) simulations verified that I^- could enter the solvation structure of Zn^{2+}. Furthermore, density functional theory (DFT) calculations based on the Marcus theory were applied for analyzing the I^- involved interfacial electrochemical reaction process of Zn deposition. The results identified the crucial role of I^- in regulating the early-stage Zn nucleation and growth process, by accelerating the initial heterogeneous Zn nucleation process and modulating the initial Zn growth orientation, eventually leading to the Zn plating with the dominating Zn (002) orientation. Therefore, the Zn‖copper (Cu) battery showed superior coulombic efficiency (CE) (an initial CE of 99.9% and an average CE of 99.9% over 50 cycles at 10 mA cm^{-2}). Moreover, the assembled anode-free Zn‖iodine battery exhibited outstanding cycling stability and high-rate performance over 10 000 cycles at 50 mA cm^{-2} (0.99 mA h cm^{-2} capacity output and 88.2% capacity retention).

Results and discussion

Initially, the deposition behavior of Zn on the surface of Cu foil was investigated in a 2 M zinc sulfate ($ZnSO_4$) electrolyte with various concentrations of LiI additive (specifically 0, 0.1, 0.25, 0.5, and 1 M) under the deposition conditions of 10 mA cm^{-2} and 5 mA h cm^{-2}. Scanning electron microscopy (SEM) results (Fig. S2a–e, ESI†) clearly revealed that in the absence of the LiI additive, the Zn plating exhibited a loose, porous, and irregular morphology. In contrast, with the addition of LiI, the Zn plating showed a laminar stacking morphology, and with increasing the LiI concentration, the gaps amid layers gradually diminished. When the LiI concentration exceeded 0.5 M, the Zn plating exhibited a blocky morphology. Meanwhile, X-ray diffraction (XRD) patterns signified that the relative intensity of the Zn (002) crystal plane within the Zn plating incrementally increased with increasing LiI additive concentration (Fig. S3a and b, ESI†). This evolution was quantified by calculating the peak ratio (R) of the Zn (002) crystal plane to the Zn (100) crystal plane, which culminated at 0.5 M LiI (Fig. S4, ESI†). As prior research has shown that the preferential orientation of the Zn (002) crystal plane can effectively restrain dendritic growth and side reactions,[25–27] the $ZnSO_4$ electrolyte with a 0.5 M LiI additive was chosen as the primary focus of our study. Comparative experiments were also conducted to investigate the deposition behavior of Zn on the surface of Cu foil under the same deposition conditions in the $ZnSO_4$ electrolyte with different concentrations of other iodide salts (specifically NaI, KI, and ZnI_2) and various concentrations of lithium sulfate (Li_2SO_4) additives (Fig. S5–S7, ESI†). The results demonstrated that it is the I^- ions that are primarily associated with the preferential orientation of the Zn (002) crystal plane rather than the lithium ions (Li^+). Real-time evolution of the deposition and dissolution processes of Zn on

the surface of Cu foil was investigated using *in situ* optical microscopy (Fig. S8, ESI†). In the $ZnSO_4$ electrolyte, Zn deposition/dissolution exhibited distinctively different behavior and morphology with visibly undissolved "dead Zn" during the dissolution process. However, in the LiI–$ZnSO_4$ electrolyte, uniform morphology was observed during the Zn deposition and dissolution, indicating superior reversibility in the first deposition/dissolution cycle. The reversibility of the first Zn deposition/dissolution cycle is crucial, as undissolved "dead Zn" can further cause non-uniform deposition and degrade the electrode/electrolyte interfacial stability in subsequent cycles.

An in-depth investigation into the regulation of I^- on the solvation structure of Zn^{2+} and the electrode/electrolyte interface prior to the Zn deposition/dissolution process was conducted. To begin with, the impact of LiI additives on the solvation structure of Zn^{2+} was examined. Across various LiI concentrations, no notable shifts were observed in the bending vibration peak of O–H and the stretching vibration peak of sulfate anions (SO_4^{2-}) according to the ATR-FTIR spectra (Fig. 1a). Raman spectra also exhibited similar features as shown in Fig. 1b. The impact of I^- on the solvation structure of Zn^{2+} was then further examined in detail through ^1H NMR. As shown in Fig. 1c, the ^1H peak position in pure D_2O was at 4.699 ppm, shifting to 4.695 ppm upon addition of an equivalent volume of pure water. Following the addition of 2 M $ZnSO_4$, the peak shifted to 4.718 ppm, indicating a decrease in the surrounding electron density and the weakening of shielding for protons in the water, suggesting a reduction in the content of free water molecules.[28–30] Upon further addition of varying amounts of LiI (from 0.1 M to 1 M), the ^1H peak gradually shifted to lower values, indicating the release of some coordination water molecules in the solvation structure of Zn^{2+}. This could be attributed to the I^- ions entering the solvated structure of Zn^{2+} and replacing some of the coordinated water molecules.[31] In

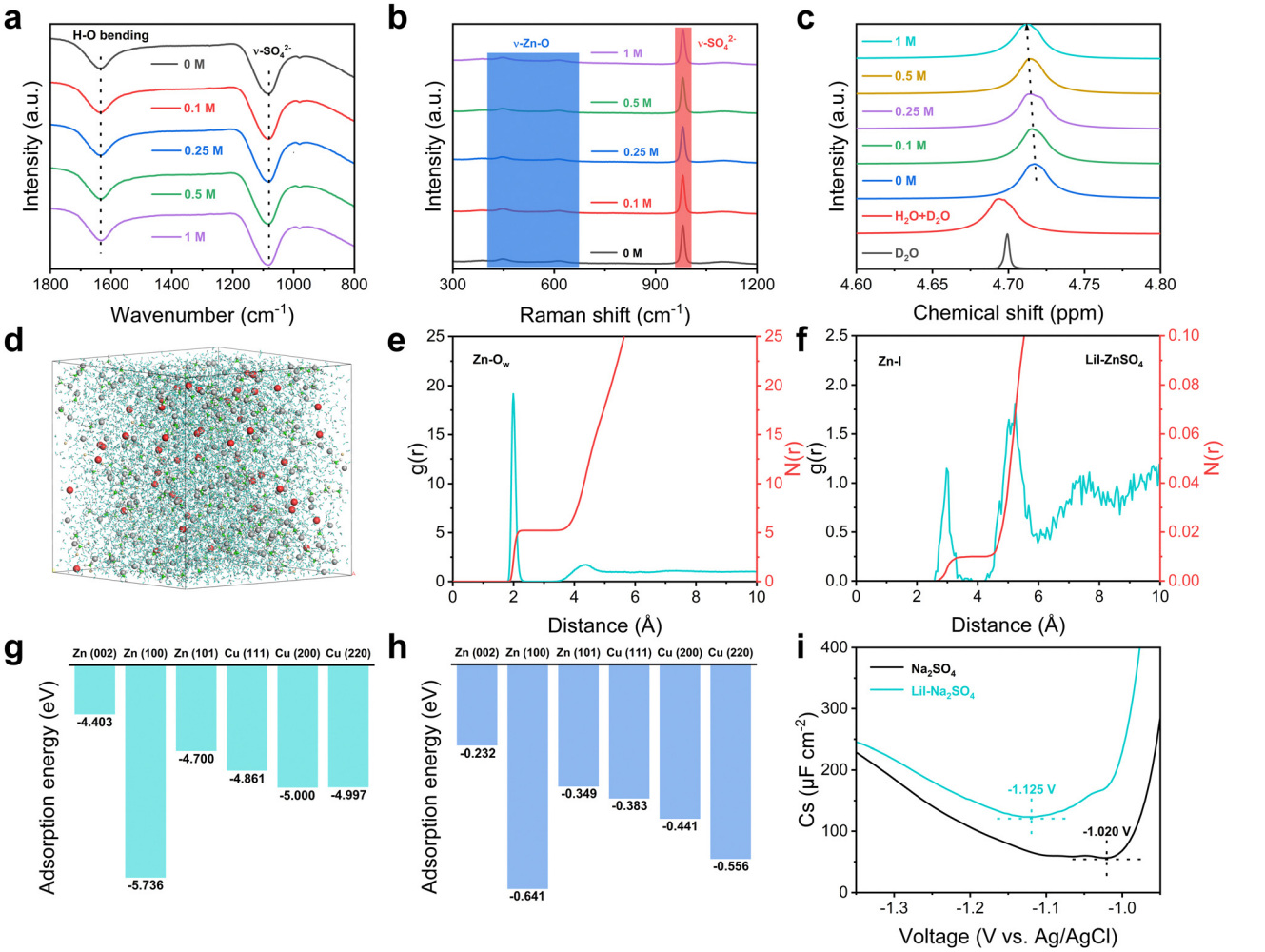

Fig. 1 Regulation of the Zn^{2+} solvation structure and the electrode/electrolyte interface by LiI. (a) ATR-FTIR spectra, (b) Raman spectra, and (c) ^1H NMR spectra of the $ZnSO_4$-based electrolyte with various concentrations of LiI additives. (d) MD snapshots of the LiI–$ZnSO_4$ electrolyte. Zn, I, S, O, Li, and H atoms are represented by gray, red, green, white, yellow, and cyan balls, respectively. The water molecules are represented by a stick-and-stick model. (e) RDF and the coordination number of Zn–O_w. (f) RDF and the coordination number of Zn–I. (g) The adsorption energies of I^- on different crystal planes of Zn and Cu. (h) The adsorption energies of H_2O on different crystal planes of Zn and Cu. (i) Differential capacitance curves for Zn in the Na_2SO_4 electrolyte with or without LiI.

addition, the negatively charged I^- exhibited a stronger interaction with Zn^{2+}, as reflected by the much lower binding energy compared to that between H_2O and Zn^{2+} (Fig. S9, ESI†). Furthermore, MD simulations were conducted to investigate the evolution of the solvation structure of Zn^{2+} (Fig. 1d and Fig. S10, ESI†). The primary solvation structure was deduced to be $Zn(H_2O)_6^{2+}$ in the pristine $ZnSO_4$ electrolyte, with an average coordination distance of 1.99 Å (Fig. S10, ESI†). The addition of 0.5 M LiI slightly decreased the coordination number $N(r)$ of Zn–O_w from 5.28 to 5.22 (Fig. 1e and Fig. S11, ESI†), where O_w represents the oxygen atom in the water molecule. Meanwhile, a Zn–I coordination structure emerged, with a coordination peak at 2.98 Å and an $N(r)$ of 0.01 (Fig. 1f). Therefore, it could be concluded that I^- could enter the solvation structure of Zn^{2+} to form $ZnI(H_2O)_5^+$, consistent with the previously reported literature.[27,32] However, the fraction of $ZnI(H_2O)_5^+$ in the bulk electrolyte might be small. Furthermore, an investigation was conducted on the influence of I^- on the EDL at the electrode surface by DFT calculations. Initially, the adsorption energies of I^- and water molecules on the three principal crystal planes of Zn and Cu metals were calculated (Fig. 1g and h). Fig. S12 and S13 (ESI†) illustrate the adsorption models of I^- and water molecules on different crystal planes of Zn and Cu metals, respectively. The results demonstrated the markedly lower adsorption energies for I^- compared to water molecules on all the principal crystal planes of either Zn or Cu. Moreover, I^- exhibited higher adsorption energies on the Zn (002) crystal plane, in contrast to the Zn (100) and Zn (101) crystal planes. This suggested that I^- ions were preferentially adsorbed onto the Zn (100) and Zn (101) crystal planes. In addition, the differential capacitance curves further confirmed the adsorption behavior of I^- on the surface of Zn metal. The LiI–Na_2SO_4 electrolyte showed a larger capacitance value and a pronounced negative shift from −1.020 to −1.125 V in the potential of zero charge (PZC) of the Zn metal surface (Fig. 1i) compared to the Na_2SO_4 only electrolyte, where the PZC represents the potential at the minimum capacitance. This shift in the PZC should be ascribed to the intrinsic adsorption phenomenon by negatively charged I^- ions.[33] Based on the above results, we speculated that the mechanism by which I^- regulated Zn deposition behavior was mainly related to the preferential adsorption of I^- at the electrode interface to form an I^--rich EDL and the preferred adsorption of I^- on certain crystal planes to regulate the Zn growth orientation.

Zn‖Cu batteries were assembled to further explore the influence of I^- on the electrochemical reaction kinetics of Zn deposition/dissolution on the surface of Cu metal. According to the cyclic voltammetry (CV) results, upon the introduction of LiI additive, the reaction current density significantly increased, accompanied by a notable decrease in the nucleation overpotential value of Zn from 0.065 V to 0.029 V in the first cycle (Fig. 2a and Fig. S14, ESI†), indicating that the LiI additive significantly enhanced the kinetics of Zn deposition/dissolution. Furthermore, the Tafel curves exhibited consistent findings. In the LiI–$ZnSO_4$ electrolyte, the exchange current density surged to 7.685 mA cm^{-2}, exhibiting a notable increase compared to the 0.090 mA cm^{-2} observed in the $ZnSO_4$ electrolyte (Fig. 2b). Chronoamperometry (CA) experiments were conducted to further investigate the Zn deposition behavior (Fig. 2c). In the $ZnSO_4$ electrolyte, when applying a −100 mV overpotential, the current density continued to increase within 200 seconds, indicating a growth mechanism being primarily governed by 2D diffusion of Zn^{2+}. In contrast, in the LiI–$ZnSO_4$ electrolyte, the Zn deposition behavior transitioned from the initial 2D diffusion of Zn^{2+} to the 3D diffusion of Zn^{2+} within the first few seconds and subsequently maintained a stable current density. Meanwhile, in the LiI–$ZnSO_4$ electrolyte, the current density was significantly higher than that in the $ZnSO_4$ electrolyte, further confirming the capability of I^- in accelerating the kinetics of Zn deposition. In addition, we also studied the CV (Fig. S15a and b, ESI†), Tafel (Fig. S16a and b, ESI†), and CA (Fig. S17a and b, ESI†) results on other halide anions as the additives, such as chloride ions (Cl^-) and bromide ions (Br^-). Both Cl^- and Br^- demonstrated the capability to accelerate the reaction kinetics of Zn deposition/dissolution and reduce the nucleation overpotential value of Zn, being similar to I^-. Meanwhile, their accelerating effects followed the order $I^- > Br^- > Cl^-$. Furthermore, the reversibility of the Zn deposition/dissolution process was investigated in $ZnSO_4$ electrolytes with and without LiI, under the specific conditions of 10 mA cm^{-2} and 5 mA h cm^{-2}. Based on the actual weight of the Zn foil, the calculated actual utilization rate of Zn foil was approximately 53.8%. The Zn‖Cu battery delivered a high average coulombic efficiency (CE) of 99.9% during 50 cycles in the electrolyte with LiI, with an initial CE (ICE) of 99.9% (Fig. 2d). The CE values demonstrated in our work have significantly exceeded the values reported in previous literature (Fig. S18, ESI†). In contrast, the ICE was only 97.1% in the electrolyte without LiI. Furthermore, the voltage hysteresis between charging and discharging decreased from 102.0 mV without LiI to 77.5 mV with LiI (Fig. 2e). As depicted in Fig. 2f, the charge–discharge curve was obviously abnormal after 16 cycles in the electrolyte without LiI, whereas a relatively stable charge–discharge curve was maintained even after 50 cycles in the electrolyte with LiI. Furthermore, optical images after 10 cycles revealed a significant black residue on the surface of the Cu foil in the $ZnSO_4$ electrolyte, while the Cu foil surface remained bright in the LiI–$ZnSO_4$ electrolyte (Fig. S19a and b, ESI†), which suggested the introduction of I^- inhibiting the formation of ''dead Zn''. Similar tests were also conducted in the Li_2SO_4–$ZnSO_4$ electrolyte to eliminate the influence of Li^+ (Fig. S20a and b, ESI†). The results showed a relative improvement in the cycling stability of the Zn‖Cu battery, but no significant enhancements were observed in polarization and ICE. Furthermore, the rate capability of Zn‖Zn batteries in two electrolytes was tested. The results demonstrated that the Zn‖Zn battery could easily withstand a high current density of 50 mA cm^{-2} in the LiI–$ZnSO_4$ electrolyte, while this was unattainable in the $ZnSO_4$ electrolyte (Fig. 2g). Long-term cycling tests revealed that the Zn‖Zn battery exhibited excellent stability in the LiI–$ZnSO_4$ electrolyte, maintaining stable cycling for 400 hours. However, its cycling life fell short of 100 hours in the $ZnSO_4$ electrolyte (Fig. 2h). Additionally, characterization of the Zn anode after cycling

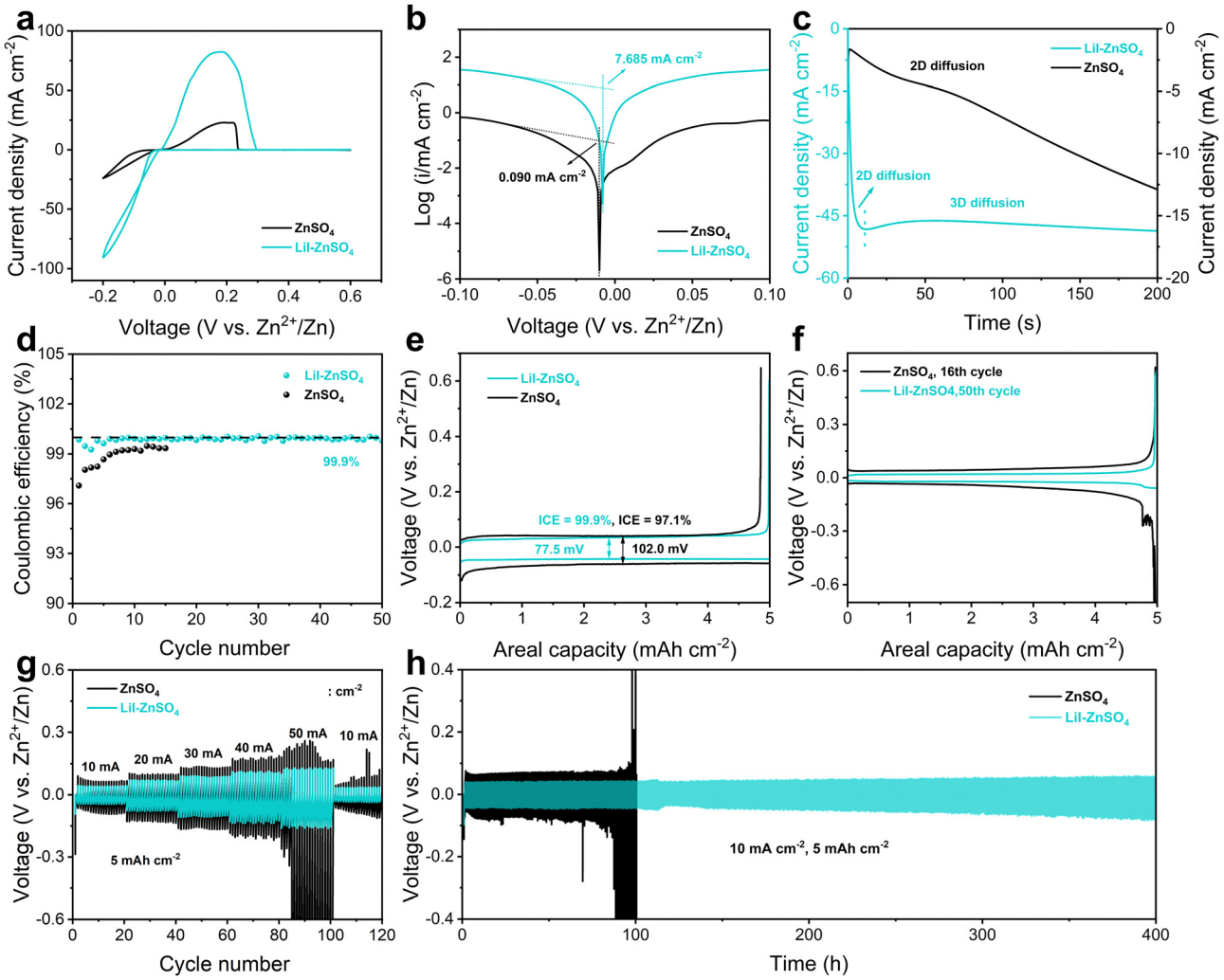

Fig. 2 Electrochemical performances of the Zn deposition/dissolution processes in the electrolyte with and without LiI. (a) CV curves of Zn‖Cu batteries in the first cycle. (b) Tafel curves of Zn‖Zn batteries. (c) CA curves of Zn‖Zn batteries at −100 mV. (d) CE of Zn‖Cu batteries. (e) and (f) Charge and discharge curves of Zn‖Cu batteries. (g) Rate capabilities of Zn‖Zn batteries. (h) Long-term galvanostatic charging/discharging of Zn‖Zn batteries.

indicated that I^- regulation effectively reduced dendrite formation and side reactions (Fig. S21a–f, ESI†). The above results indicated that I^- significantly enhanced the kinetics of Zn deposition/dissolution, reduced the nucleation overpotential of Zn, and markedly improved the reversibility, cycling stability, and rate capability of the Zn anode.

To further understand the I^- regulation mechanism of the interfacial electrochemical reaction process that occurred during Zn deposition, the energy barriers during the electrochemical reaction process were studied *via* DFT calculations. According to the Marcus theory, the reduction reaction of Zn^{2+} is hypothesized to involve two main processes. In the first process, solvated Zn^{2+} accepts electrons to form monovalent Zn^+ intermediates, which then undergo desolvation. In the second process, these desolvated intermediates are then adsorbed onto the substrate surface for the subsequent reduction and deposition. The first process is generally considered the rate-determining step. Therefore, our focus was to understand the regulation mechanism of I^- in the first step reduction process of Zn^{2+}. Fig. 3a depicts the Gibbs activation free energy curve for the Zn^{2+} reduction reaction process in the LiI–$ZnSO_4$ electrolyte. Initially, the solvated Zn^{2+} underwent recombination with the solvated sheathing layer, while simultaneously experiencing an electron transition, resulting in the formation of the active intermediate $ZnI(H_2O)_5$. This intermediate subsequently underwent a desolvation process and then was adsorbed onto the substrate surface for the electron transfer and deposition process. The Gibbs activation free energy of the charge transfer process ($\Delta G_1^{\ddagger}$) was calculated using the four-point method based on the Marcus theory, as illustrated in Fig. 3b.[34,35] The Gibbs activation free energy of the desolvation process ($\Delta G_2^{\ddagger}$) was determined by calculating the energy difference between solvated and desolvated structures. The structures of key intermediates for two electrolytes are also presented in Fig. S22a–f (ESI†). For the $ZnSO_4$ electrolyte, previous studies indicated that the charge transfer process of Zn^{2+} involved the participation of OH^- to stabilize the active Zn^+ intermediate.[36] That means in the Marcus charge transfer process, the electron first transfers from H_2O to Zn^{2+} *via* the Zn–OH bonds, leading to

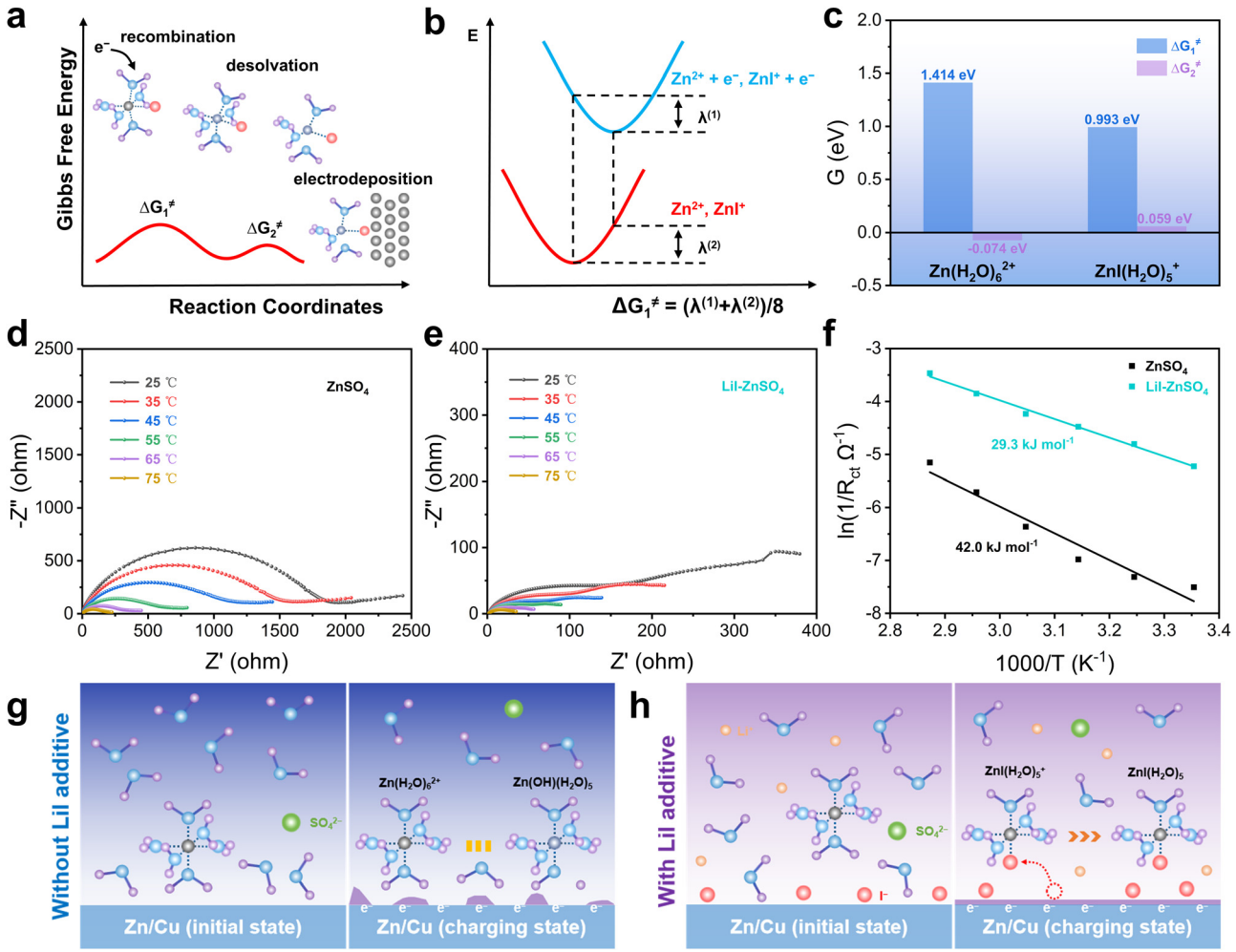

Fig. 3 Mechanism investigation of the I^- involved interfacial electrochemical reaction process on the Zn anode. (a) Schematic illustration of the interfacial electrochemical reaction process in the LiI–$ZnSO_4$ electrolyte (according to the Marcus charge transfer process and the desolvation process). (b) Schematic illustration of the calculation method for the energy barriers in the Marcus charge transfer process. (c) The calculated Gibbs activation free energy. (d) and (e) EIS of the Zn electrodes in the electrolytes with and without LiI at different temperatures. (f) The calculated activation energies of both Zn electrodes in symmetric batteries by using the Arrhenius equation. Schematic illustration for the Zn^{2+} charge transfer process in the electrolyte (g) without or (h) with the LiI additive.

the disruption of the H–OH bond within the coordination water molecule and the formation of the $Zn(OH)(H_2O)_5$ intermediate, followed by a subsequent desolvation process.[37] Fig. 3c illustrates the corresponding calculated Gibbs activation free energy associated with this process. It is worth noting that the $\Delta G_2^{\ddagger}$ of the $Zn(OH)(H_2O)_5$ intermediate was calculated to be less than 0, indicating the spontaneous nature of the desolvation process. According to the calculated Gibbs activation energy value, the underlying mechanism for the accelerated kinetics of Zn deposition in the LiI–$ZnSO_4$ electrolyte might lie in the significant reduction of the Marcus charge transfer energy barrier from Zn^{2+} to Zn^+ ($\Delta G_1^{\ddagger}$). In addition, the Gibbs activation free energies of the above process were also calculated similarly by replacing I^- with other halide ions Cl^- and Br^-, as illustrated in Fig. S23 (ESI†). The corresponding structures of key intermediates are depicted in Fig. S24a–f (ESI†). Comparing the Gibbs activation free energy for the different solvation structures of $Zn(H_2O)_6^{2+}$ and $ZnX(H_2O)_5^+$ (X = I, Br, Cl), it could be generally deduced that the accelerated kinetics of Zn deposition by halide ions might stem from their significant reduction of their Marcus charge transfer energy barrier from Zn^{2+} to Zn^+. However, the variation in kinetics acceleration by different halide ions could be attributed to the difference in their desolvation energy barriers.

Furthermore, the variable-temperature electrochemical impedance spectroscopy (EIS) method was also employed to investigate the kinetics of Zn deposition. The Zn‖Zn batteries in the LiI–$ZnSO_4$ electrolyte exhibited a significantly smaller semicircle, representing a smaller interfacial charge transfer resistance (Fig. 3d and e), which is because the I^--rich EDL reduces the spontaneous corrosion and I^- ions lower the charge transfer energy barrier while maintaining a low desolvation energy barrier for Zn^{2+}, thereby accelerating the charge transfer kinetics at the interface of the Zn anode (Fig. S25a–c, ESI†). The Arrhenius equation can be used to analyze the activation energy, E_a, as follows:

$$\frac{1}{R_{ct}} = A\exp\left(-\frac{E_a}{R\times T}\right)$$

where R_{ct} represents the interfacial resistance, A denotes the frequency factor, R is the gas constant and T indicates the absolute temperature.[38,39] The calculation showed a lower activation energy E_a (29.3 kJ mol^{-1}) in the LiI–$ZnSO_4$ electrolyte compared to the $ZnSO_4$ electrolyte (42.0 kJ mol^{-1}) (Fig. 3f), indicating that the Zn deposition barrier in the former was significantly lower than that in the latter. Furthermore, distribution of relaxation times (DRT) analysis was conducted on the charge transfer process of Zn^{2+} in two electrolytes (Fig. S26a and b, ESI†). The low log[$\tau(s)$] region corresponded to the zinc hydroxide sulfate (ZHS, $Zn_4SO_4(OH)_6{\cdot}xH_2O$) by-products, and the intermediate log[$\tau(s)$] region encompassed the charge transfer process of Zn^{2+}, including the adsorption and desolvation of Zn^{2+}, as well as the migration of Zn^{2+}, Zn^+, and Zn^0.[40,41] Meanwhile, the high log[$\tau(s)$] region was associated with the diffusion of active Zn^{2+}. It was evident that two types of diffusion existed in the high log[$\tau(s)$] region in the electrolyte containing LiI, and we hypothesized that one of them may be related to the I^--coordinated hydrated Zn^{2+}.[42]

Based on the experimental results and theoretical calculation results presented above, we can propose the potential mechanisms for the charge transfer process of Zn^{2+} in electrolytes with and without the LiI additive. As illustrated in Fig. 3g, in the pristine $ZnSO_4$ electrolyte, a water-rich inner Helmholtz layer is initially formed on the substrate surface due to the polarizing effect of water molecules. During charging, electrons accumulated on the substrate surface are transferred to Zn^{2+} *via* the Zn–OH bonds in the coordination water molecule. This transfer process causes the breaking of the H–OH bond, resulting in the formation of the $Zn(OH)(H_2O)_5$ intermediate. However, this process is hindered by the high Marcus charge transfer energy barrier, resulting in a slow reaction rate. In addition, the nucleation growth of Zn atoms shows irregular deposition behavior due to the absence of any discernible preferred orientation. On the other hand, as illustrated in Fig. 3h, with the introduction of LiI additive, the adsorption of I^- transforms the originally water-rich inner Helmholtz layer into an I^--rich inner Helmholtz layer. During the charging process, the $Zn(H_2O)_6^{2+}$ driven by the electric field coordinates with interfacial I^- to form $ZnI(H_2O)_5^+$ complexes. Subsequently, electrons are transferred through the Zn–I bond, leading to the formation of the $ZnI(H_2O)_5$ intermediate. Due to a notably reduced Marcus charge transfer energy barrier, this process is rapid and so effectively accelerates the reaction kinetics of initial heterogeneous Zn nucleation. With the electrodeposition continuing, at the early stage of Zn plating, due to the tendency of I^- to be adsorbed on the Zn (100) and Zn (101) crystal planes compared to the Zn (002) plane, the Zn growth onto these crystal planes is promoted. The crystal growth theory suggests that crystal planes with faster growth rates tend to be prone to being overlapped by adjacent crystal planes, resulting in their shrinkage or even disappearance.[43,44] This eventually leads to the Zn plating with the dominating Zn (002) orientation. Overall, we can deduce that the regulation of early-stage Zn nucleation and growth by I^- contributes to achieving highly reversible Zn deposition/dissolution, thus holding great potential for high-performance anode-free AZMBs.

Furthermore, the commercial activated carbon (AC) as the cathode iodine carrier and commercial Cu foil as the anode Zn carrier, with the incorporated electrochemically active I^- and Zn^{2+} from the LiI–$ZnSO_4$ electrolyte were assembled to an anode-free Zn‖iodine battery (also referred to as Cu‖AC). As the active Zn^{2+} and I^- are both from the electrolyte rather than from either electrode, this test can be showcased as the prototype for an anode-free Zn‖iodine flow battery. Initially, the reaction kinetics of this system was investigated through CV curves at varied scan rates. The CV curves predominantly exhibited a pair of redox peaks corresponding to the single-electron transfer process of I^- (Fig. 4a). Moreover, the peak currents (i_p) and scan rates (ν) in CV tests follow the formula:

$$i_p = a\nu^b$$

where a represents a constant and b is interpreted as the slope of the fitted line.[45] When the b value approaches 0.5, it indicates a diffusion-controlled process, while the b value approaching 1.0 suggests a capacitive-controlled process. As shown in Fig. 4b, it could be observed that the b values for the pair of redox peaks in this system are both approaching 0.5, implying that the primary electrochemical reaction in this system is diffusion-controlled. The contribution ratio of capacitive-controlled processes to diffusion-controlled processes was further calculated (Fig. S27, ESI†). This suggested that the energy storage mechanism of the system was primarily attributed to the Faraday battery reaction of I^- to iodine atoms (I^0), rather than a non-Faraday capacitive reaction related to AC. Furthermore, the rate performance test on the Cu‖AC battery at current densities of 10, 20, 30, 40, and 50 mA cm^{-2} was conducted, revealing approximate areal capacities of 1.60, 1.51, 1.43, 1.37, and 1.31 mA h cm^{-2}, respectively. Converting these values based on the mass of AC yielded mass-specific capacities of 140.3, 132.5, 126.0, 120.6, and 115.2 mA h g_{AC}^{-1} (Fig. 4c). The corresponding rate curves indicated minimal voltage hysteresis, suggesting the exceptional high-rate performance for this system (Fig. 4d). Additionally, the Cu‖AC battery maintained an areal capacity of 1.59 mA h cm^{-2} after 1000 cycles at 10 mA cm^{-2}, corresponding to a mass-specific capacity of 131.5 mA h g_{AC}^{-1} and a capacity retention of 92.8% (Fig. 4e). The gradual increase in initial capacity could be attributed to the progressive wetting of the AC electrode and the removal of oxygen functional groups, which corresponded to the gradual improvement in electrode reaction kinetics (Fig. S28 and S29, ESI†).[46] Moreover, SEM and transmission electron microscopy of Cu foil and AC before and after cycling were conducted, as shown in Fig. S30a–f and S31 (ESI†). Furthermore, it also delivered 0.99 mA h cm^{-2} after 10 000 cycles, corresponding to a mass-specific capacity of 84.8 mA h g_{AC}^{-1}, with an 88.2% retention at an ultra-high current density of 50 mA cm^{-2} (Fig. 4f). Conversely, the Cu‖AC battery assembled with the $ZnSO_4$ electrolyte exhibited near zero capacity attenuation after less than 100 cycles at 10 mA cm^{-2} (Fig. S32, ESI†). Additionally, pouch Cu‖AC batteries with capacities of 28.5 mA h (4 × 4 cm^2) and 82.4 mA h (8 × 8 cm^2) exhibited excellent cycling stability, retaining 75.7% and 71.6% of their capacities after 200 and 500 cycles, respectively (Fig. S33a and b, ESI†).

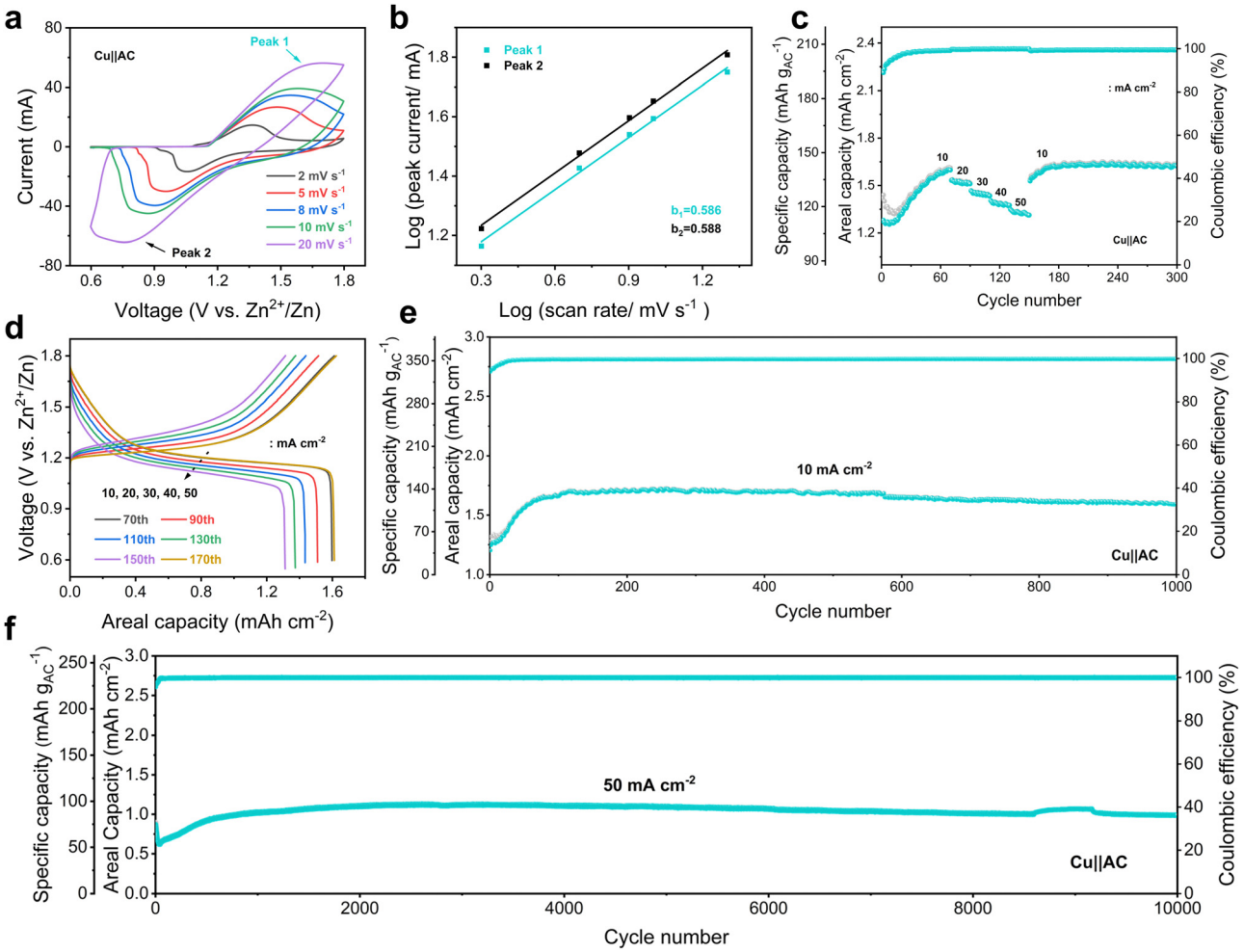

Fig. 4 Electrochemical performances of anode-free Zn‖iodine batteries. (a) CV curves of the Cu‖AC battery at varied scan rates. (b) The correlation between peak currents and scan rates. (c) Rate capability of the Cu‖AC battery and (d) the corresponding charge and discharge curves at varied cycling numbers. (e) Cycling performance of the Cu‖AC battery at 10 mA cm^{-2}. (f) Cycling performance of the Cu‖AC battery at 50 mA cm^{-2}.

In addition, commercial activated carbon cloth (ACC) as a cathode iodine carrier was applied to study the evolution of anode during the operation of the Cu‖ACC full battery in the $ZnSO_4$ electrolyte with LiI. The optical photos in Fig. S34a–f (ESI†) reveal the reversible formation and disappearance of Zn deposits with the charge/discharge process, mirroring the corresponding XRD patterns in Fig. S35 (ESI†). Interestingly, the by-product ZHS also exhibited similar changes and the reversible formation and disappearance during the charge and discharge process. In addition, the energy-dispersive X-ray spectroscopy mapping and the corresponding atomic content analyses of elements aligned well with the XRD results (Fig. S36 and Table S1, ESI†). In particular, the iodine element was clearly detected on the surface of Cu foil during the Zn deposition process but vanished upon Zn dissolution, confirming the active participation of I^- during the Zn deposition process. In summary, on the anode side, the I^- regulation on the electrochemical reaction interface enables the highly reversible Zn deposition/dissolution on the surface of Cu foil, whereas on the cathode side, I^- serves as the redox-active species. The highly reversible and high-rate aqueous anode-free Zn-iodine battery demonstrates its significant potential for practical applications, particularly in anode-free Zn-based flow batteries.

Conclusions

In conclusion, an innovative approach to achieve high-performance anode-free AZMBs was demonstrated by simply adding LiI as the additive into the electrolyte. The underlying mechanism of I^- regulating the early-stage Zn nucleation and growth process was identified by experimental results and theoretical calculations. Initially, the formation of an I^--rich electrochemical double layer reduces the Marcus charge transfer energy barrier of Zn^{2+} ions, hence significantly lowering the heterogeneous nucleation overpotential of Zn. Subsequently, I^- ions are preferentially adsorbed onto the Zn (100) and Zn (101) crystal planes compared to the Zn (002) plane, thereby promoting the Zn growth onto these two planes and leading to the Zn plating with the dominating Zn (002) orientation. As a result,

the assembled Zn‖Cu asymmetric batteries demonstrated an extremely high CE (99.9% of ICE and 99.9% of average CE during 50 cycles at 10 mA cm^{-2}). Furthermore, the assembled anode-free Zn‖iodine battery exhibited superior cycling stability and high-rate performance, with a maintained capacity of 0.99 mA h cm^{-2}, corresponding to an 88.2% retention after 10 000 cycles at 50 mA cm^{-2}. This work provides valuable insights into the electrochemical reaction interface regulation of anode-free AZMBs, where I^- ions at the interface effectively regulate the early-stage Zn nucleation and growth, leading to a highly reversible and high-rate Zn anode. This approach demonstrated can also be applied to other anode-free metal batteries.

Author contributions

W. S. conducted the experiments, conceptualized data management, developed formal analysis methods, and drafted the initial manuscript. Z. S. and W. Z. provided support for the computational aspects, with Z. S. contributing the majority of the work. S. L. and F. H. reviewed and edited the manuscript. Q. A. and Q. L. supervised the experiments, revised the content, and finalized the manuscript for submission.

Data availability

The data supporting this article have been included as part of the ESI.†

Conflicts of interest

There are no conflicts to declare.

Acknowledgements

W. S. and Z. S. are the co-first authors of the article. This work was supported by the National Natural Science Foundation of China (52072285, 52172231 and 51972259) and the Natural Science Foundation of Hubei Province (2022CFA087).

Notes and references

1 L. E. Blanc, D. Kundu and L. F. Nazar, *Joule*, 2020, **4**, 771–799.
2 W. Nie, H. Cheng, Q. Sun, S. Liang, X. Lu, B. Lu and J. Zhou, *Small Methods*, 2024, **8**, 2201572.
3 Z. Yi, G. Chen, F. Hou, L. Wang and J. Liang, *Adv. Energy Mater.*, 2021, **11**, 2003065.
4 H. Jia, Z. Wang, B. Tawiah, Y. Wang, C.-Y. Chan, B. Fei and F. Pan, *Nano Energy*, 2020, **70**, 104523.
5 W. Du, E. H. Ang, Y. Yang, Y. Zhang, M. Ye and C. C. Li, *Energy Environ. Sci.*, 2020, **13**, 3330–3360.
6 Q. Yang, Q. Li, Z. Liu, D. Wang, Y. Guo, X. Li, Y. Tang, H. Li, B. Dong and C. Zhi, *Adv. Mater.*, 2020, **32**, 2001854.
7 F. Ming, Y. Zhu, G. Huang, A.-H. Emwas, H. Liang, Y. Cui and H. N. Alshareef, *J. Am. Chem. Soc.*, 2022, **144**, 7160–7170.
8 Y. Zhu, Y. Cui and H. N. Alshareef, *Nano Lett.*, 2021, **21**, 1446–1453.
9 Q. Zhang, J. Luan, Y. Tang, X. Ji and H. Wang, *Angew. Chem., Int. Ed.*, 2020, **59**, 13180–13191.
10 C. Liu, X. Xie, B. Lu, J. Zhou and S. Liang, *ACS Energy Lett.*, 2021, **6**, 1015–1033.
11 B. Li, X. Zhang, T. Wang, Z. He, B. Lu, S. Liang and J. Zhou, *Nano-Micro Lett.*, 2022, **14**, 1–31.
12 A. Bayaguud, X. Luo, Y. Fu and C. Zhu, *ACS Energy Lett.*, 2020, **5**, 3012–3020.
13 L. Miao, R. Wang, S. Di, Z. Qian, L. Zhang, W. Xin, M. Liu, Z. Zhu, S. Chu, Y. Du and N. Zhang, *ACS Nano*, 2022, **16**, 9667–9678.
14 W. Xu, K. Zhao, W. Huo, Y. Wang, G. Yao, X. Gu, H. Cheng, L. Mai, C. Hu and X. Wang, *Nano Energy*, 2019, **62**, 275–281.
15 X. Zeng, K. Xie, S. Liu, S. Zhang, J. Hao, J. Liu, W. K. Pang, J. Liu, P. Rao, Q. Wang, J. Mao and Z. Guo, *Energy Environ. Sci.*, 2021, **14**, 5947–5957.
16 P. Biswal, S. Stalin, A. Kludze, S. Choudhury and L. A. Archer, *Nano Lett.*, 2019, **19**, 8191–8200.
17 A. Pei, G. Zheng, F. Shi, Y. Li and Y. Cui, *Nano Lett.*, 2017, **17**, 1132–1139.
18 P. Biswal, A. Kludze, J. Rodrigues, Y. Deng, T. Moon, S. Stalin, Q. Zhao, J. Yin, L. F. Kourkoutis and L. A. Archer, *Proc. Natl. Acad. Sci. U. S. A.*, 2021, **118**, e2012071118.
19 Y. Zhang, L. Wang, Q. Li, B. Hu, J. Kang, Y. Meng, Z. Zhao and H. Lu, *Nano-Micro Lett*, 2022, **14**, 208.
20 Y. An, Y. Tian, K. Zhang, Y. Liu, C. Liu, S. Xiong, J. Feng and Y. Qian, *Adv. Funct. Mater.*, 2021, **31**, 2101886.
21 L. Cao, D. Li, T. Pollard, T. Deng, B. Zhang, C. Yang, L. Chen, J. Vatamanu, E. Hu, M. J. Hourwitz, L. Ma, M. Ding, Q. Li, S. Hou, K. Gaskell, J. T. Fourkas, X.-Q. Yang, K. Xu, O. Borodin and C. Wang, *Nat. Nanotechnol.*, 2021, **16**, 902–910.
22 R. A. Marcus, *J. Chem. Phys.*, 1956, **24**, 966–978.
23 P. Quaino, E. Colombo, F. Juarez, E. Santos, G. Belletti, A. Groß and W. Schmickler, *Electrochem. Commun.*, 2021, **122**, 106876.
24 L. M. C. Pinto, E. Spohr, P. Quaino, E. Santos and W. Schmickler, *Angew. Chem., Int. Ed.*, 2013, **52**, 7883–7885.
25 H. Zhang, Y. Zhong, J. Li, Y. Liao, J. Zeng, Y. Shen, L. Yuan, Z. Li and Y. Huang, *Adv. Energy Mater.*, 2023, **13**, 2203254.
26 T. Wei, Y. Ren, Y. Wang, L. e Mo, Z. Li, H. Zhang, L. Hu and G. Cao, *ACS Nano*, 2023, **17**, 3765–3775.
27 W. Yuan, X. Nie, Y. Wang, X. Li, G. Ma, Y. Wang, S. Shen and N. Zhang, *ACS Nano*, 2023, **17**, 23861–23871.
28 N. Dubouis, A. Serva, E. Salager, M. Deschamps, M. Salanne and A. Grimaud, *J. Phys. Chem. Lett.*, 2018, **9**, 6683–6688.
29 N. Chang, T. Li, R. Li, S. Wang, Y. Yin, H. Zhang and X. Li, *Energy Environ. Sci.*, 2020, **13**, 3527–3535.
30 J. Hao, L. Yuan, C. Ye, D. Chao, K. Davey, Z. Guo and S. Z. Qiao, *Angew. Chem., Int. Ed.*, 2021, **60**, 7366–7375.
31 Q. Zhang, Y. Ma, Y. Lu, Y. Ni, L. Lin, Z. Hao, Z. Yan, Q. Zhao and J. Chen, *J. Am. Chem. Soc.*, 2022, **144**, 18435–18443.
32 Q. Zhang, K. Xia, Y. Ma, Y. Lu, L. Li, J. Liang, S. Chou and J. Chen, *ACS Energy Lett.*, 2021, **6**, 2704–2712.
33 C. Huang, X. Zhao, S. Liu, Y. Hao, Q. Tang, A. Hu, Z. Liu and X. Chen, *Adv. Mater.*, 2021, **33**, 2100445.

34 S. F. Nelsen, S. C. Blackstock and Y. Kim, *J. Am. Chem. Soc.*, 1987, **109**, 677–682.
35 F. Wang, H. Hua, D. Wu, J. Li, Y. Xu, X. Nie, Y. Zhuang, J. Zeng and J. Zhao, *ACS Energy Lett.*, 2022, **8**, 780–789.
36 J. Agrisuelas, G.-J. Juan José, D. Gimenez-Romero and F. Vicente, *Electrochim. Acta*, 2009, **54**, 6046–6052.
37 F. Zhang, T. Liao, H. Peng, S. Xi, D.-C. Qi, A. Micallef, C. Yan, L. Jiang and Z. Sun, *J. Am. Chem. Soc.*, 2024, **146**, 10812–10821.
38 X. Xie, S. Liang, J. Gao, S. Guo, J. Guo, C. Wang, G. Xu, X. Wu, G. Chen and J. Zhou, *Energy Environ. Sci.*, 2020, **13**, 503–510.
39 H. Qiu, X. Du, J. Zhao, Y. Wang, J. Ju, Z. Chen, Z. Hu, D. Yan, X. Zhou and G. Cui, *Nat. Commun.*, 2019, **10**, 5374.
40 M. Yan, C. Xu, Y. Sun, H. Pan and H. Li, *Nano Energy*, 2021, **82**, 105739.
41 S. Wang, Y. Zhao, H. Lv, X. Hu, J. He, C. Zhi and H. Li, *Small*, 2023, 2207664.
42 H. Wang, X. Feng, Y. Chen, Y.-S. Liu, K. S. Han, M. Zhou, M. H. Engelhard, V. Murugesan, R. S. Assary, T. L. Liu, W. Henderson, Z. Nie, M. Gu, J. Xiao, C. Wang, K. Persson, D. Mei, J.-G. Zhang, K. T. Mueller, J. Guo, K. Zavadil, Y. Shao and J. Liu, *ACS Energy Lett.*, 2019, **5**, 200–206.
43 M. Qiu, P. Sun, Y. Wang, L. Ma, C. Zhi and W. Mai, *Angew. Chem., Int. Ed.*, 2022, **61**, e202214654.
44 W. Yuan, X. Nie, G. Ma, M. Liu, Y. Wang, S. Shen and N. Zhang, *Angew. Chem., Int. Ed.*, 2023, **62**, e202218386.
45 J. Liu, J. Wang, C. Xu, H. Jiang, C. Li, L. Zhang, J. Lin and Z. X. Shen, *Adv. Sci.*, 2018, **5**, 1700322.
46 S. T. Senthilkumar, R. K. Selvan, Y. S. Lee and J. S. Melo, *J. Mater. Chem. A*, 2013, **1**, 1086–1095.